Available online at www.sciencedirect.com
ScienceDirect
Trans. Nonferrous Met. Soc. China 34(2024) 2575−2588
Transactions of Nonferrous Metals Society of China
www.tnmsc.cn

Evading strength−ductility trade-off of GH605 alloy using magnetic field-assisted undercooling treatment

Yi-xuan HE[1,2,3,4], Fan BU[1,2], Zhang-chi BIAN[1,2], Ming-xiu XIANG[1], Meng-meng ZHOU[1], Xu-dong LIU[1], Lei ZHU[5], Jun WANG[1], Jin-shan LI[1]

1. State Key Laboratory of Solidification Processing, Northwestern Polytechnical University, Xi'an 710072, China;
2. Center of Advanced Lubrication and Seal Materials, Northwestern Polytechnical University, Xi'an, 710072, China;
3. Collaborative Innovation Center of NPU, Shanghai 201108, China;
4. Institute of Superconducting Materials and Applied Technology, Northwestern Polytechnical University, Xi'an 710072, China;
5. Shaanxi Key Laboratory of Electrical Materials and Infiltration Technology, Xi'an University of Technology, Xi'an 710048, China

Received 16 January 2023; accepted 7 June 2023

Abstract: Undercooling solidification under a magnetic field (UMF) is an effective way to tailor the microstructure and properties of Co-based alloys. In this study, by attributing to the UMF treatment, the strength−ductility trade-off dilemma in GH605 superalloy is successfully overcome. The UMF treatment can effectively refine the grains and increase the solid solubility, leading to the high yield strength. The main deformation mechanism in the as-forged alloy is dislocation slipping. By contrast, multiple deformation mechanisms, including stacking faults, twining, dislocation slipping, and their strong interactions are activated in the UMF-treated sample during compression deformation, which enhances the strength and ductility simultaneously. In addition, the precipitation of hard Laves phases along the grain boundaries can be obtained after UMF treatment, hindering crack propagation during compression deformation.
Key words: undercooling treatment; magnetic field; GH605 alloy; strengthening mechanisms

1 Introduction

GH605 (L-605), nominally Co−20Cr−15W−10Ni, is a kind of typical solid-solution strengthening Co-based superalloy. It has been developed for high temperature load-bearing applications because of excellent combination of mechanical strength and creep resistance. Nevertheless, due to the insufficient strengthening effect of the solid-solution strengthening, the limited strength of GH605 is still an issue. Although some of ordered phases precipitated within the alloy matrix (such as Co_7W_6, and Co_2W) are expected to enhance the strength [1,2], this approach requires long-term aging time (nearly 1000 h), which restricted the application in the industrial field.

The constitution, selection and growth of multi-phases in the superalloy during the non-equilibrium process are very complicated, and it is the complex microstructures that provide new opportunities for the design of excellent structural materials [3−5]. Previous research results [6,9] have demonstrated that the solidification microstructure of multi-component alloys is strongly related to the alloy composition, temperature gradient, cooling rate and supercooling degree. Generally, the metal melt would nucleate and grow in an undercooled

Corresponding author: Yi-xuan HE, Tel: +86-18792688654, E-mail: yxhe@nwpu.edu.cn
DOI: 10.1016/S1003-6326(24)66561-1

way thermodynamically, forming the distinctive undercooled microstructure. Subsequently, various phenomena are observed, such as modification of the precipitations and morphology, which in turn have significant effect on the mechanical properties. For instance, WANG et al [6] optimized the morphology of the second phase in the Ni−Zr alloy by means of undercooling treatment, thereby prolonging the uniform deformation stage. ZHANG and WANG [7] obtained hard and stable Fe_2B phases in Fe-based amorphous composite during rapid solidification, as a result, the hardness and elastic modulus of the alloy were enhanced. ZHANG et al [8] found that the undercooled K4169 alloy at large undercooling exhibited the optimization of tensile strength (932.2 MPa) and elongation (6.5%), ascribing to the uniform distribution of Laves phase as well as the decrease of grain size and intergranular phase fractions. Unfortunately, the undercooled solidified microstructure exhibits an inevitable inhomogeneity with the micro-segregation, crack, holes, and shrinkage cavity during metallurgy process [9], thus deteriorating the final properties of products significantly.

Recently, imposing a magnetic field during the material processing has been proved to be adequate for manipulating the defects during solidification such as dislocations, stack faults and twins, which could provide possibilities for excitation of the multiple deformation mechanisms, resulting in an excellent performance [10]. SHAO et al [11] found that the magnetic field could promote the dislocation slipping and reduce dislocation density around the grain boundaries in tempered 20Cr2Ni4A alloy, which results in a decrease of residual stress and an enhanced mechanical performance. WANG et al [12] proved that the application of the high magnetic field could optimize the hardness and ultimate tensile strength of M50 bearing steel during tempering (530 °C) due to the dislocation strengthening. LUO et al [13] found that the Sn−Bi solder solidified under magnetic field exhibits the refiner β-Sn dendrites, which affects the density of moving dislocations and achieves high resistance to stress and strain relaxation. LUO eat al [14] also pointed out that the coarse dendritic transformed into the fine rosette with the application of pulsed magnetic field in AZ80 magnesium alloy, enhancing the plasticity of the ingot center by more than 80%. Except for those, the magnetic field could also manipulate the physical properties of alloys. For instance, ZUO et al [15] fabricated the Fe−Sn monotectic alloys with increasing magnetic anisotropy, ascribed to the formation of the aligned microstructure. Therefore, the method of magnetic field-assisted material processing shows great potentials for performance optimization and industry application. Subsequently, the mechanical strength of GH605 superalloy is unarguably promising to be further tuned by the undercooling treatment under the magnetic field.

In the present work, the undercooling treatment under strong magnetic field (UMF treatment) was used to regulate the microstructure evolution and mechanical properties of the GH605 superalloy. The extraordinary combination of strength and ductility was obtained after UMF treatment, and then the strengthening mechanisms were in-depth investigated.

2 Experimental

Material used in this work is commercial Co-based superalloy GH605. The alloy was processed into several cylinders with the size of 40 mm in length and 20 mm in radius, which were subsequently ground, ultrasonic cleaned and then sealed into the quartz tubes as candidate samples. In order to prevent oxidation, the candidate samples were covered by the B_2O_3 flux. The tubes were placed in a homemade resistance heating furnace that is equipped in a superconducting magnet. The details of the facility are available in Ref. [16]. The flux was dehydrated at 1050 K for 6 h in advance.

Each sample was cyclically heated and cooled down several times for achieving a large undercooling ΔT. The 10 T static strong magnetic field was applied on the final heating−cooling cycle of melts. Then, the samples were water-quenched at about 1000 K. The cylindrical specimens (d5 mm × 10 mm) were uniaxially compressed along the direction of magnetic field and forged at room temperature with a constant strain rate of $1\times10^{-3}\ s^{-1}$. The uniaxial compression tests were performed in an Instron 8502 testing machine and graphite powder was used as lubricant during deformation process to achieve relatively homogeneous deformation. The nano-hardness of phases was explored by nano-indentation (Hysitron

TI 980 system) with a Berkovich tip. The load force and duration time in nano-indentation test were set as 10 mN and 50 s, respectively. For the further microstructure characterization, the UMF-treated samples were cut along the direction of magnetic field, and the deformed samples were sectioned along the direction of compression.

The phase constitutions and morphologies were analyzed by SEM (FEI Quanta 650 F) and attached energy dispersive X-ray spectrometry (EDS) system. The samples were ground up to 4000-grit SiC sand paper followed by mirror polished for the SEM observation. The transmission electron microscopy (TEM) lamellas were prepared by two methods in the present work. To analyze the element composition and crystallographic structure of specified phase, the TEM lamellas were lifted out from the mirror polished surface by using a dual-beam focused ion beam (FIB) workstation (FEI Helios Nanolab 600), and the final thinning was selected as a low Ga and current of 80 pA. The lamellas for the strengthening mechanism research were prepared by hand grinding to a thickness of 50 μm. Then, a twin jet polishing technique was applied with an alcohol solution containing 10% perchloric acid at −30 °C and 20 V condition to obtain the thin samples. TEM observations were conducted under a FEI Themis Z microscope equipped with double spherical aberration corrector operating at 300 kV.

3 Results and discussion

3.1 Original microstructure

Figure 1(a) shows the typical backscattered electron (BSE) micrograph of the as-forged GH605 alloy. It can be noted that the microstructure consists of equiaxed recrystallized grains and a few annealing twins. Based on the statistical results by Image Pro software, the average grain size of the as-forged alloy is about 53.4 μm (more than 500 grains without considering twin boundaries). Figure 1(b) shows the partial enlarged view of Fig. 1(a). There are a few globular precipitates distributed around the grain boundaries, with the diameter of about 500 nm. To characterize those precipitates in detail, a TEM lamella was lift-out by the FIB technology from the location indicated in Fig. 1(b), and the corresponding bright-field (BF) image is shown in Fig. 1(c). The Points *d* and *e* in Fig. 1(c) correspond to the matrix and the precipitate, respectively. Based on the selected area electron diffraction (SAED) patterns analysis in Figs. 1(d) and (e), it can be inferred that both the precipitate and the matrix are FCC structures. Figures 1(f) and (g) show the compositions of the precipitate and the matrix, respectively. For the precipitate, the specific atomic ratio of Co to W to Cr to C is estimated to be 0.28:0.32:0.24:0.13, close to that of the M_6C compound [17]. Therefore, combining the SAED pattern and elemental composition, these precipitates are preliminarily identified as the $(CoCrW)_6C$ carbide, which was also observed in other Co-based superalloys. For the matrix, the EDS result in Fig. 1(g) is consistent with the nominal composition of GH605 alloy.

3.2 Microstructure evolution

Figure 2(a) shows the BSE image of GH605 alloy subjected to undercooling treatment. Obviously, the grain morphology and the characteristics of precipitates are completely different from that of the as-forged alloy. The microstructure was occupied with fully equiaxed grains, and the average grain size is decreased to 15.1 μm. Moreover, a lot of island-shaped intergranular phases precipitate around grain boundaries. To further identify the intergranular secondary-phases, Figs. 3(a, b) show the high angle angular dark field (HAADF) images and elemental distribution maps of the alloy after undercooling treatment. It can be noted that these island-shaped secondary-phases are rich in W, Cr and Co solutes. Region 1 and Region 2 in Fig. 3(a) correspond to the matrix and the secondary phase, respectively. By means of the SAED analysis in Fig. 3(c), it can be known that the matrix shows FCC structure. The SAED pattern in Fig. 3(d) indicates that the crystal structure of the secondary phase is determined to be HCP structure, with lattice parameters measured as a=(10.86±0.03) Å, and c=(19.25±0.02) Å, approximately. The EDS spectra in Figs. 3(e) and (f) further present the elemental composition of the two phases. The specific atomic ratio of Co to W to Cr to Ni in the secondary phase is ~48:26:22:3 (Table 1), close to that of the $Co_{23}Cr_{15}W_{15}$ compound. Thus, both the elemental composition and SAED pattern certify that the secondary-phases belong to C15-Laves phase with HCP structure. The element composition of matrix (Fig. 1(g)) is

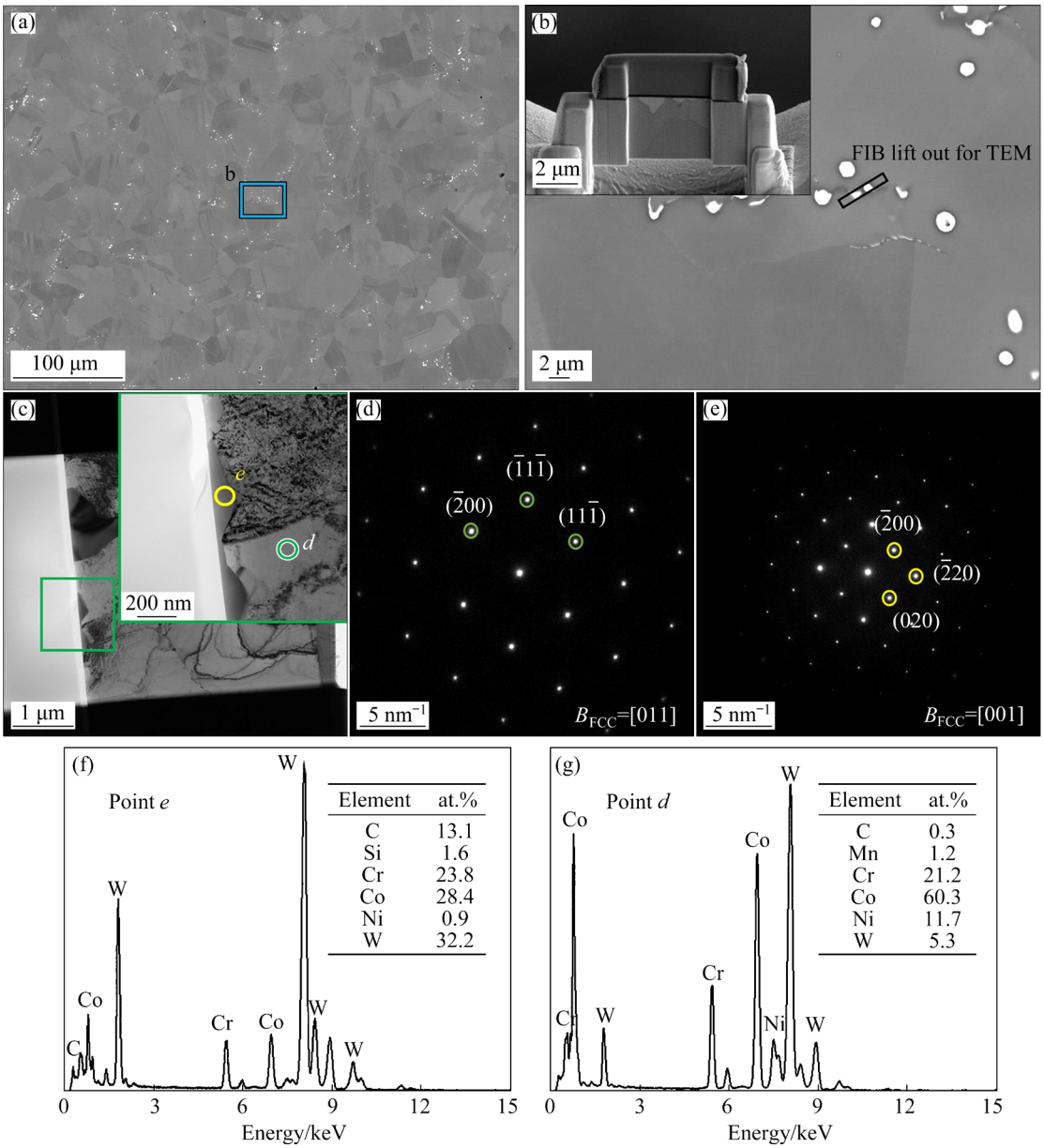

Fig. 1 Initial microstructure of forged GH605 alloy: (a) Backscattered electron micrograph; (b) Enlarged segment in Fig. 1(a) showing location for preparing TEM lamella by FIB; (c) TEM bright-field image of precipitate in Fig. 1(b); (d, e) SAED patterns obtained at locations indicated by circles *d* and *e* in Fig. 1(c), respectively; (f, g) Elemental compositions of precipitate and matrix shown in Fig. 1(c) , respectively

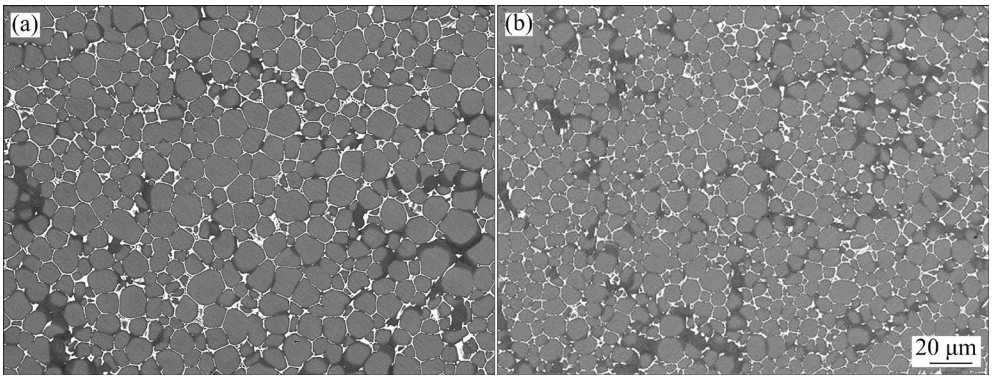

Fig. 2 Backscattered electron micrographs of GH605 alloy after undercooling treatment (a) and UMF treatment (b)

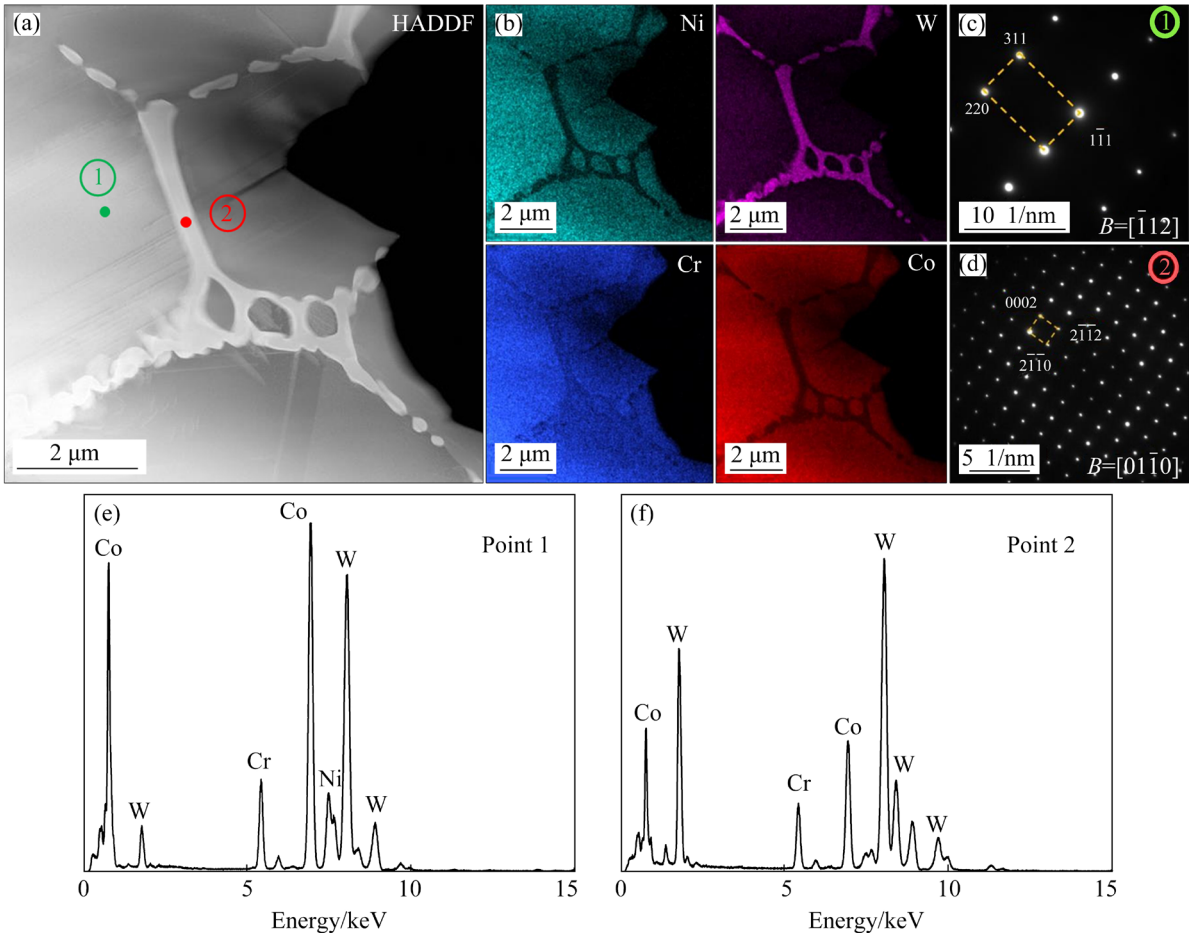

Fig. 3 Microstructure of GH605 alloy after undercooling treatment: (a) HADDF image; (b) Corresponding EDS elemental maps; (c, d) SAED patterns of matrix (Region 1) and secondary-phase (Region 2) in Fig. 3(a), respectively; (e, f) EDS spectra of matrix (Region 1) and secondary-phase (Region 2) obtained from Fig. 3(a), respectively

Table 1 Elemental compositions of points in Fig. 3(a) (at.%)

Element	FCC matrix (Point 1)	Laves phase (Point 2)
Cr	21.80±0.25	23.21±0.30
Mn	0.29±0.06	0.20±0.03
Co	58.43±0.14	48.20±0.11
Ni	14.28±0.19	2.78±0.23
W	5.20±0.05	25.61±0.08

also similar to the nominal composition of GH605 alloy (Ni: 50%−60%; Cr: 20%−25%; Co: 10%−20%; Fe<10%), which is not affected after the undercooling treatment.

After the undercooling treatment, the network (W,Cr)-rich Laves phase precipitated continuously along the boundaries of the FCC matrix, rather than the refined isolated precipitates composed of $(CoCrW)_6C$ carbides in the as-forged alloy. It is reasonable that for the as-forged alloy under a near-equilibrium solidification, the Cr, W and C elements are mainly enriched in the precipitate while Co and Ni segregate to the FCC matrixes, which attributes to the lower formation energies of MC carbides (M is W and Cr) and the C solute could diffuse sufficiently, forming the stable carbides [18]. Under the undercooling treatment of non-equilibrium solidification, the solute trap will take place if the solidification plateau is too short for the atomic diffusion, thus causing the chemical segregation. It is worth noting that the solidification segregation of alloying elements often determines the final solidification path of superalloys [19]. Without sufficient time for diffusion, the chemical distribution of the C solute would be more homogeneous, instead of forming the carbides locally, resulting in the disappearance of the carbides precipitation. Moreover, the solidification segregation of heavy W solutes is also alleviated, that is, the chemical compositions within the

inter-dendrite regions therefore would be tailored and a new phase should form. JOHANNES et al [20] studied the relationship between the Laves phase containing transition metal and its average valence electron concentration (N), and they found that C15-Laves phase has the most stable structure when $3.4 \leq N \leq 4.9$ and $6.5 \leq N \leq 7.7$. The value of N is expressed as

$$N=\sum_i C_i N_i \quad (1)$$

where C_i is the mole fraction, and N_i is effective valence electron of single element. Hereinto, in our system, the N value of inter-dendrite HCP phase is estimated to be 7.56, which approves for the formation of C15-type Laves phases owing to the modified chemical segregation induced by the undercooling treatment. Therefore, the solidification sequence of the experimental undercooled alloy can be denoted as: liquid → FCC + liquid → FCC + C15-Laves.

Figure 2(b) shows the BSE image of GH605 alloy subjected to UMF treatment. Similar to the undercooling treated alloy (Fig. 2(a)), the microstructure of UMF-treated alloy is also filled with equiaxed grains, and a lot of island-shaped secondary-phases appeared around grain boundaries. Nevertheless, the grain size of the alloy after UMF treatment is further decreased to 5.7 μm, which is obviously smaller than that of the as-forged and undercooled alloy. To characterize secondary phases, a TEM lamella was lifted out using FIB technology as indicated in Figs. 4(a) and (b). Figure 4(c) shows the enlarged view of the region highlighted in Fig. 4(b). The Points *a* and *b* in Fig. 4(c) correspond to the secondary-phase and matrix, respectively. According to the SAED analysis in Figs. 4(d) and (e), it can be determined that the precipitate and matrix remain HCP and FCC structures, respectively. The elemental compositions of the secondary-phase and matrix are listed in Table 2, which are consistent with the results in Table 1. This suggests that these island-shaped secondary-phases obtained by UMF treatment are still C15-Laves phase. Therefore, UMF treatment can further refine the grains on basis of undercooling treatment and obtain the C15-Laves phase.

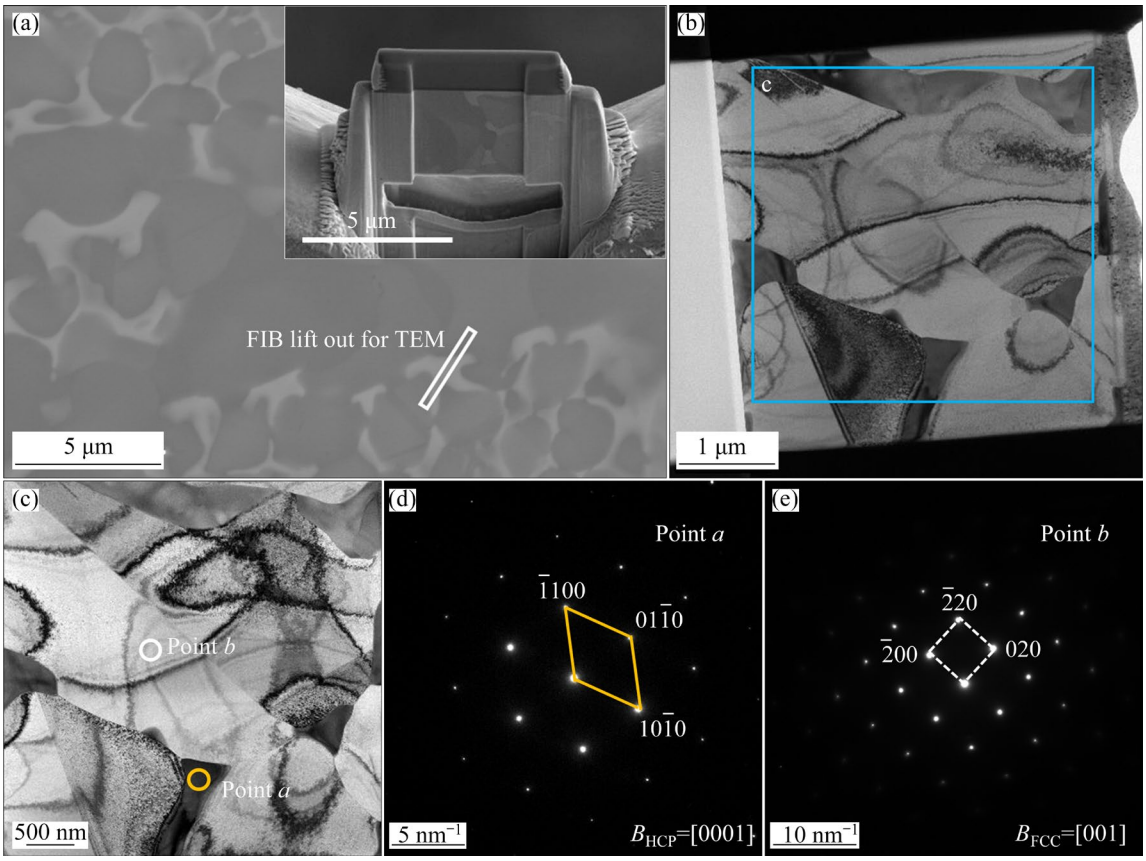

Fig. 4 Microstructure of GH605 alloy after UMF treatment: (a) Backscattered electron micrograph showing location for preparing TEM lamella by FIB; (b) TEM bright-field image of precipitate in Fig. 2(a); (c) Enlarged segment in Fig. 2(b); (d, e) SAED patterns obtained at locations indicated by Points *a* and *b* in Fig. 4(c), respectively

Table 2 Elemental compositions of points in Fig. 4(c) (at.%)

Element	Laves phase (Point *a*)	Matrix (Point *b*)
Cr	21.88±0.28	22.88±0.34
Mn	0.30±0.07	0.29±0.05
Co	45.30±0.18	57.54±0.21
Ni	5.70±0.26	12.57±0.22
W	26.82±0.04	6.72±0.07

It has been well accepted that the strong magnetic field could refine the grains effectively during solidification process. The reasons may lie in two aspects below. (1) The thermal gradient along the solid−liquid interface, together with the divergence of thermo-physical properties between solid and the melt, could lead to the occurrence of Seebeck effect and therefore the formation of thermoelectric currents. Coupled with the external magnetic field, the thermoelectric magnetic forces (TEMF) are produced within the solid and melts, which causes the apparent torque and strong stresses (e.g., up to 10^8 N/m^2 for Al−Cu alloy [21]). As a result, the fragmentation and grain refinement occur. The similar phenomena were also reported in other alloys like Zn−Ag [22] and Ni-based DZ417G superalloy [23]. (2) The plastic strains accumulated between liquid flow and solid skeleton, as the driving force, could induce the recrystallization process of the structure in the post-recalescence period [24]. When the external magnetic field is applied, the recrystallization could be accelerated, ascribing to the enhanced driving force (i.e., TEMF) for recrystallization during undercooling process. Hence, more recrystallized refined grains form by magnetic field, which also happens in the Co−B systems [25].

3.3 Mechanical properties

Figure 5(a) displays the engineering stress−strain curves of GH605 alloy at room temperature (RT) with different preparation methods, showing the mechanical properties including yield strength (σ_y), ultimate compression strength (σ_{UCS}) and total elongation (ε_T). Apparently, the overall performances of the UMF-treated alloy are superior to those of the as-forged and undercooling treated alloy, and the corresponding mechanical properties are listed in Table 3. The σ_y, σ_{UCS} and ε_T of the as-forged alloy are (565±9) MPa, (2177±20) MPa and (31.7±2.3)%, respectively. For undercooled alloy without magnetic field, the σ_y, σ_{UCS}, and ε_T rise to (649±13) MPa, (2710±29) MPa and (33.7±2.3)%, respectively. Furthermore, a simultaneous increase in strength and ductility has been achieved in the UMF-treated alloy with the σ_y, σ_{UCS}, and ε_T being (701±17) MPa, (3262±39) MPa, and (38.6±2.9)%, respectively.

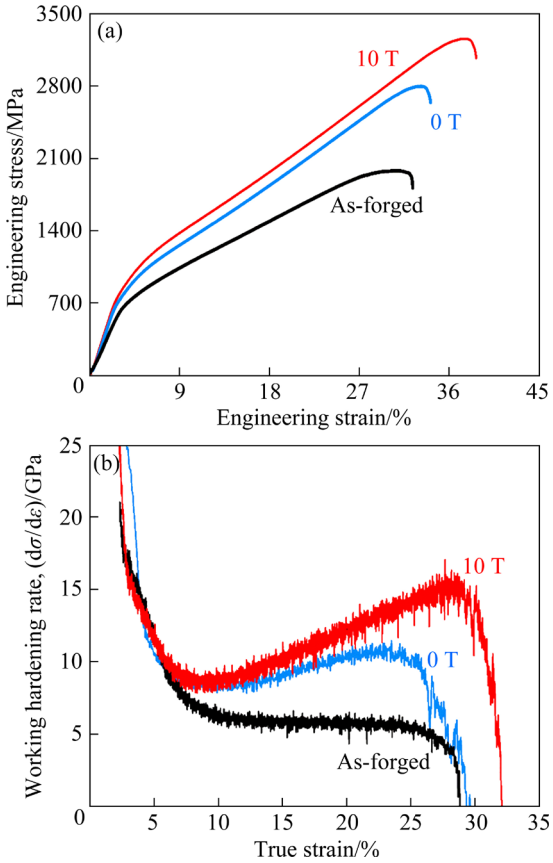

Fig. 5 Mechanical responses of GH605 alloy at different states: (a) Compression engineering stress−strain curves; (b) Corresponding strain hardening rate vs true strain curves of (a)

Table 3 Mechanical properties of GH605 alloy subjected to different treatments

Treatment	σ_y/MPa	σ_{UCS}/MPa	ε_T/%
Forging	565±9	2077±20	31.7±2.3
Undercooling	649±13	2720±29	33.9±2.5
UMF	701±17	3262±37	38.6±2.9

Figure 5(b) shows the strain hardening rate (SHR) as a function of true strain curves. For all alloys, three typical work-hardening stages could be observed. For the as-forged alloy, the SHR displays

a monotonic decrease with the increment of true strain (Stage I), which is a common result observed in metals [26]. Subsequently, the working hardening rate keeps steady (Stage II) and then decreases rapidly (Stage III) as true strain increases, denoting the fracture of alloy. Differently, the SHR in the undercooling and UMF-treated alloy is obviously elevated during the Stage II working hardening process, and then falls rapidly and fractures (Stage III). That is, the evolution of the SHR of the undercooling and UMF-treated alloy in the second stages is significantly distinctive with that of as-forge alloy, including decrease → increase → decrease. Moreover, the UMF-treated alloy has a higher strain-hardening capacity than that of the as-forged and undercooling treated alloy. It suggests that the work hardening ability increases because of different microstructure evolutions during compression deformation. To further study the underlying deformation mechanisms, the microstructures with different deformations (ε) were characterized by TEM.

3.4 Mechanisms of superior strength and ductility

The deformation microstructures at true strain ε=25% of the as-forged alloy are shown in Fig. 6. It can be observed that the microstructure is featured by dense slip bands as shown in Fig. 6(a). A partial area highlighted by the white rectangle in Fig. 6(a) was magnified and the two-beam diffraction images were carried out to further study the nature of dislocations, i.e., g=[11$\bar{1}$] and g=[110]. Lots of slip bands are seeable under g=[11$\bar{1}$] and g=[$\bar{1}$1$\bar{1}$] as illustrated in Figs. 6(b) and (d), respectively. The corresponding dark-field TEM images in Figs. 6(c) and (e) are also performed in these regions. However, only a few dislocations can be observed in Fig. 6(f) under g=[200]. According to the $g\cdot b$=0 invisibility criteria [27], the amplitude of Burgers vector of slipping dislocations is confirmed as b=a/2[01$\bar{1}$], and a is the lattice constant. Dislocations slip freely on the {111} close-packed surfaces because of the lack of barriers, which leads to the low strength [28].

The deformation substructures of the UMF alloy examined by TEM are shown in Fig. 7. At the beginning stage (ε=9%), similar to the dislocation substructures of the as-forged alloy, the plasticity is dominated by the planar dislocation slipping (Fig. 7(a)). Particularly, the extended stacking faults (SFs) with partials are observed (marked by pink arrows), which generally act as the nuclei for

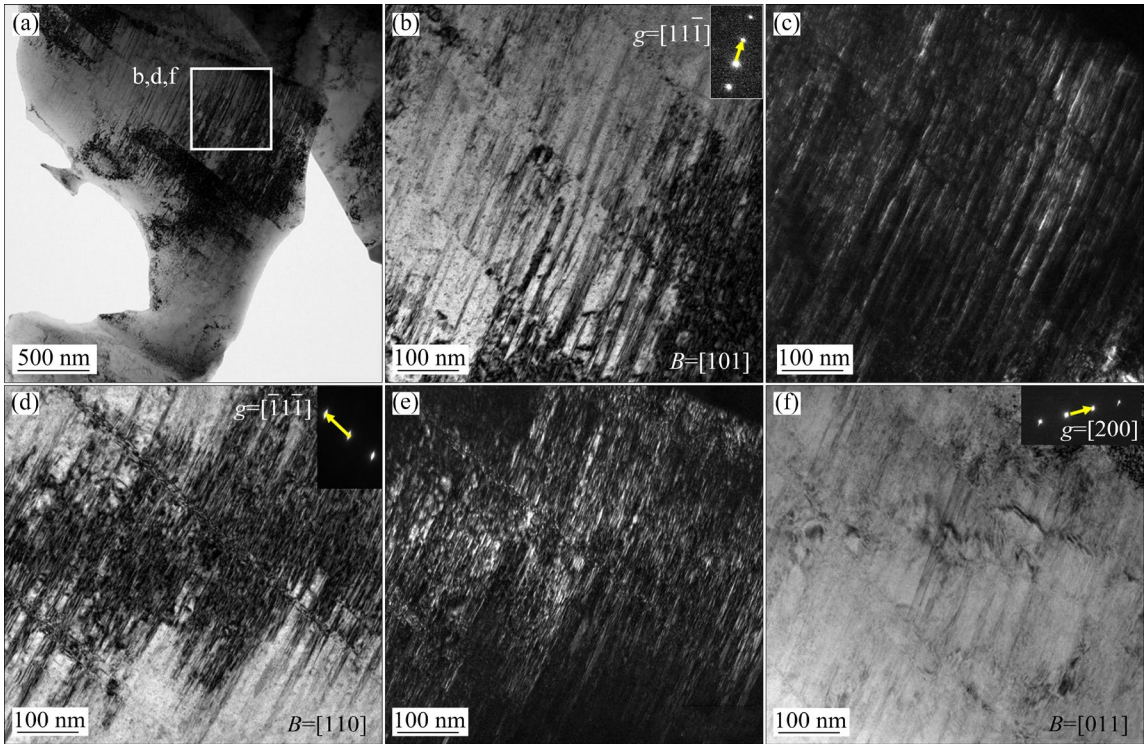

Fig. 6 Deformation substructures of as-forged GH605 alloy at true strain of 25%: (a) TEM bright-field image showing many slip bands; (b, d, f) Magnified BF images of area in (a) under g=[11$\bar{1}$], g=[$\bar{1}$1$\bar{1}$], and g=[200], respectively; (c, e) Magnified dark-field images of area in (a) under g=[11$\bar{1}$] and g=[$\bar{1}$1$\bar{1}$], respectively

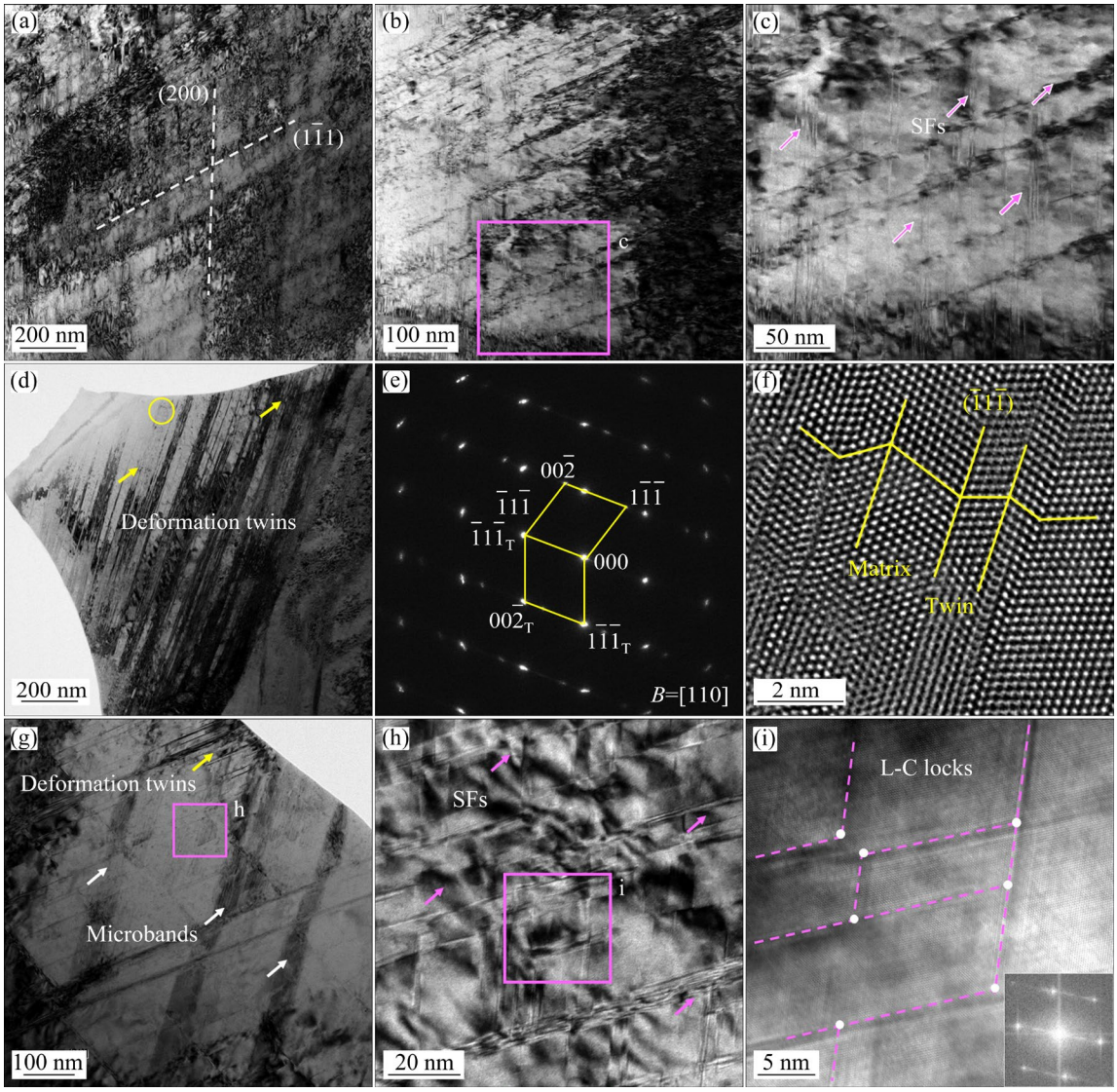

Fig. 7 Deformation substructures of UMF alloy at different true strains: (a) 9%, BF image of dislocation slipping; (b, c) 9%, extended SFs with partials (marked by pink arrows); (d) 25%, BF image of deformation twins; (e) Corresponding SAED pattern taken from region indicated by yellow circle in (d); (f) 25%, HRTEM image of deformation twins; (g) 25%, BF image of intersected deformation twins and microbands; (h) Magnified BF images of area in (g) showing SFs with high-density; (i) Magnified BF image in (h) showing Lomer−Cottrell (L−C) locks (white dots) together with SF networks (pink dash lines)

deformation twins (Figs. 7(b) and (c)). Previous studies have verified that magnetic field treatment could cause severe lattice distortion in matrix [29], which could be a possible explanation for the appearance of SFs at the initial stage of deformation [30]. With the increase of strain to 25% (Fig. 7(d)), a lot of deformation twins are detected, which dominates and acts as the important deformation mechanism. The corresponding SAED pattern and high resolution transmission electron microscope (HRTEM) image of the yellow area are illustrated in Figs. 7(e) and (f), respectively. Twinning boundaries could not only provide obstacles to impede the dislocation slipping resulting in the strengthening of the alloy [31], but introduce extra interfaces, leading to an optimized ability in accommodating plasticity [32]. In addition to deformation twins, a lot of microbands are also found (marked by white arrows), as shown in Fig. 7(g). The formation of microbands is possibly related to the grain subdivisions through dislocation cross-slip [33]. It has been proposed that microbands provide similar effects as the twinning, which optimized the strain hardening ability [34].

Therefore, the multiple deformation mechanisms including microbanding and twinning accommodate the increasing strain, which produce the rising in the SHR in the later stage of compression deformation. Figure 7(h) shows that a high density of SFs/Shockley partials appeared around deformation twins. With the increase of the length of SF bands, a lot of L−C locks form by the interaction between long and short SFs (Fig. 7(i)). L−C locks can also contribute to the increasing strain hardening. On the one hand, L−C locks obstacle the movement of dislocations. On the other hand, SF networks are established by L−C locks, which support stable substructures [35]. That is, the appearance of L−C locks also accounts for the increase of SHR.

Unlike the as-forged sample, the UMF alloy exhibits extraordinary strength and ductility, as shown in Fig. 5(a). The underlying strengthening mechanism can also be attributed to the Hall−Petch effect because of the refined grain. Based on the Hall−Petch relationship, the effect of grain size on the σ_y can be calculated as follows [36]:

$$\sigma_g=\sigma_0+k_y d^{-1/2} \quad (2)$$

where σ_g is the strength caused by grain boundary strengthening, k_y is the Hall−Petch factor, σ_0 is the frictional stress restricting the slipping of dislocations, and d is the average grain size of the alloy. In addition, the increase in strength caused by grain refinement can be described as follows:

$$\Delta\sigma_g=k_y(d_2^{-1/2}-d_1^{-1/2}) \quad (3)$$

According to the statistical results of grain size shown in Figs. 1 and 2, $\Delta\sigma_g$ of the UMF alloy is calculated to be 0.28 k_y compared with the as-forged sample. ROEBUCK et al [37] proposed that the k_y is about 200 MPa·μm$^{1/2}$ for the Co-based alloys. Thus, the strength increment introduced by grain refinement is estimated to be 56 MPa.

The total σ_y of the alloy can be calculated from the contribution of various strengthening mechanisms during plastic deformation, such as solid solution hardening (σ_s), dislocation strengthening (σ_d), precipitation strengthening (σ_p) and grain boundary strengthening (σ_g). The σ_y can be expressed as a summation of each individual contribution [38]:

$$\sigma_y=\sigma_0'+\sigma_s+\sigma_d+\sigma_g+\sigma_p \quad (4)$$

where σ_0' is the intrinsic strength or the so-called lattice fraction stress, which is a basic parameter of the alloy [39]. For the UMF-treated and as-forged alloys, the dislocation strengthening (σ_d) can be ignored since the grains are equiaxed and fully recrystallized. In addition, considering the C-15 Laves phases mainly distributed around grain boundaries, the contribution of σ_p to the σ_y of the UMF-treated alloy is negligible. The change in σ_y between UMF-treated and as-forged alloys mainly comes from the difference in σ_s and σ_g, which can be given by

$$\Delta\sigma_y=\Delta\sigma_{s(UMF/forged)}+\Delta\sigma_{g(UMF/forged)} \quad (5)$$

According to Eq. (3), the $\Delta\sigma_{HP}=\Delta\sigma_{g\ (UMF/forged)}$ is about 56 MPa. Therefore, $\Delta\sigma_y=\Delta\sigma_{s\ (UMF/forged)}+56$ MPa= 701 MPa−565 MPa=136 MPa and $\Delta\sigma_{s\ (UMF/forged)}=$ 136 MPa−56 MPa=80 MPa.

As shown in Fig. 1(g), the contents of typical solution strengthening elements, such as Mn, Cr, W and Ni in the forged matrix are 1.2 at.%, 21.2 at.%, 5.3 at.%, and 11.7 at.%, respectively. The content of Co element is 60.3 at.%. In contrast, the content of Co element in UMF-treated matrix is 57.54 at.%. The contents of Mn, Cr, W and Ni are 0.29 at.%, 22.88 at.%, 6.72 at.%, and 12.57 at.%, as listed in Table 2, which are higher than those of as-forged alloy. This indicates that the UMF-treated alloy possesses higher solid solubility within matrixes compared with the as-forged alloy, which is consistent with the higher strengthening contribution from σ_s.

3.5 Resistance to crack expansion

Figure 8 shows the nano-indentation test curves of the as-forged matrix, UMF alloy matrix and the secondary-phase, respectively. The increasing order of hardness is as follows: the as-forged matrix (6.3 GPa,) < UMF matrix (7.7 GPa) < Laves phase (8.4 GPa). Except for the inherent hard nature of Laves phase, here, the high hardness of UMF matrix is also related to the high solid solubility after UMF treatment. The change in hardness of the as-forged and UMF alloy would lead to the different compressive properties and crack propagation resistance. Figure 9 shows the fracture microstructure of the as-forged and UMF alloy. As shown in Figs. 9(a) and (b), a lot of intergranular cracks appear in the as-forged sample (marked by blue arrows). The intergranular cracks propagate smoothly without serious deflection and link up with each other, forming an interwoven cracking morphology. The fracture models in the UMF sample

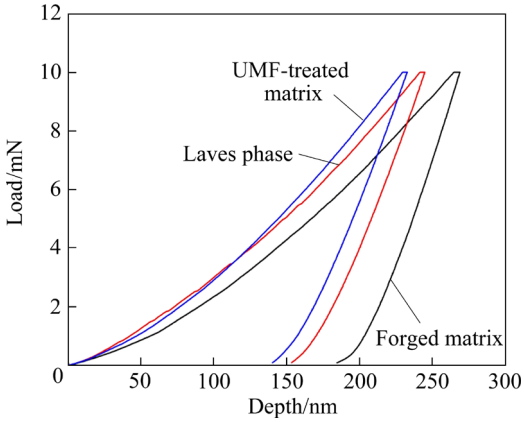

Fig. 8 Nano-indentation test curves of as-forged matrix, UMF-treated alloy matrix and secondary-phase

(Figs. 9(c) and (d)) are still characterized by typical intergranular fracture. Nevertheless, since the grain boundaries are filled with the Laves phase, the crack propagation path is tortuous and discontinuous. The formation process of intergranular fracture usually includes three stages [40]: (1) initiation of a few microcracks; (2) coalescence of microcracks; (3) continuous crack propagation until fracture. The improved ε_T of the UMF sample is primarily due to the Laves phase around grain boundaries. In the Stage (1), the grain boundaries can be strengthened by the hard Laves phases during compression deformation, as a result, the tendency for microcracks initiation is reduced. In Stages (2) and (3), compared with free crack propagation channels in the as-forged sample, intergranular Laves phases would efficiently hinder crack propagation and improve crack propagation resistance. Consequently, the UMF-treated alloy can bear more great plastic deformation before compression fracture.

4 Conclusions

(1) The UMF treatment can refine the grain efficiently and increase the solid solubility of the alloy matrix. The alloy subjected to UMF treatment shows obvious increase in yield strength ($\Delta\sigma_y$= 136 MPa), ultimate compression strength ($\Delta\sigma_{UCS}$= 1085 MPa), and elongation ($\Delta\varepsilon_T$=6.9%) compared with the as-forged sample.

(2) The main deformation mechanism of the as-forged alloy is dislocation slipping. In contrast, the high strength, elongation, and working hardening rate in the UMF-treated alloy are mainly due to the activation of the multiple deformation mechanisms, including SFs, twining, microbands, and their strong interactions. In addition, the refinement of grain size because of UMF treatment further improves strength without sacrificing ductility.

(3) Intergranular Laves-phases with a high hardness can be obtained by the UMF treatment,

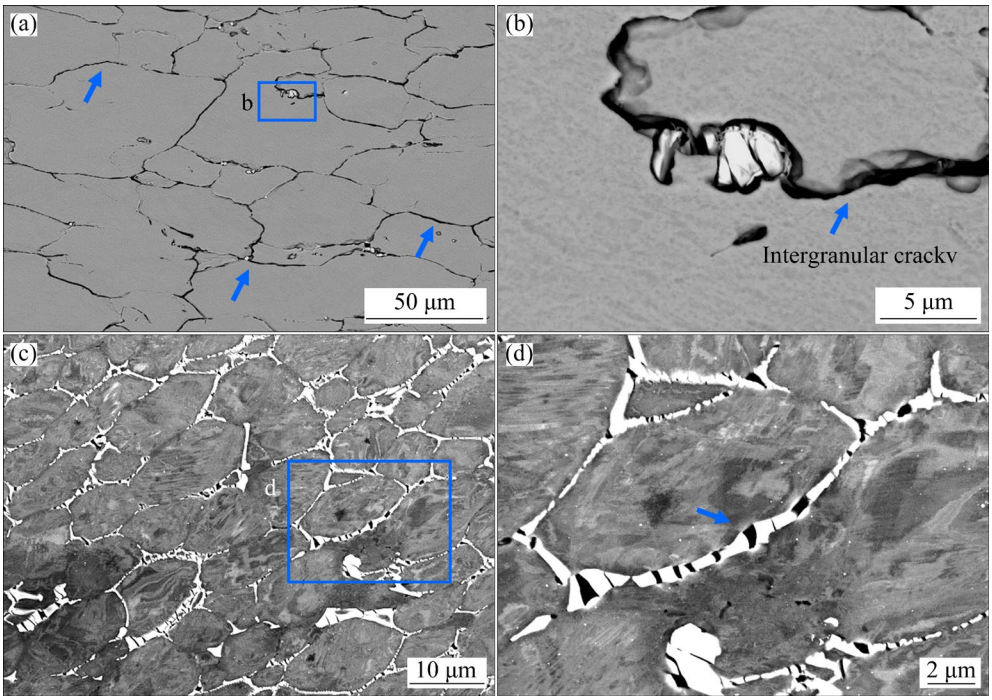

Fig. 9 Longitudinal microstructure near fractures of as-forged (a, b) and UMF (c, d) alloys

which play an important role in improving crack propagation resistance in the latter half of the compression deformation. As a result, the UMF-treated alloy can withstand great plastic deformation before fracture.

CRediT authorship contribution statement

Yi-xuan HE and **Fan BU:** Investigation, Writing – Original draft, Visualization, Formal analysis, Data curation; **Zhang-chi BIAN**, **Ming-xiu XIANG**, **Meng-meng ZHOU** and **Xu-dong LIU:** Investigation, Data curation; **Lei ZHU:** Investigation, Methodology; **Jun WANG:** Data curation, Writing – Review & editing; **Jin-shan LI:** Supervision, Funding acquisition.

Declaration of competing interest

The authors declare that they have no known competing financial interests or personal relationships that could have appeared to influence the work reported in this paper.

Acknowledgments

This work was supported by the fund of National Key Laboratory for Precision Hot Processing of Metals, China (No. 6142909200104), State Key Laboratory of Solidification Processing (NPU), China (No. 2022-TS-08), and National Training Program of Innovation and Entrepreneurship for Undergraduates. We thank Dr. ZHENG from ZKKF (Beijing) Science & Technology Company for supporting the characterization of the materials.

References

[1] SAMII ZAFARGHANDI M, ABBASI S M, MOMENI A. Effects of Nb on hot tensile deformation behavior of cast Haynes 25 Co−Cr−W−Ni alloy [J]. Journal of Alloys and Compounds, 2019, 774: 18−29.

[2] UEKI K, UEDA K, NARUSHIMA T. Microstructure and mechanical properties of heat-treated Co−20Cr−15W−10Ni alloy for biomedical application [J]. Metallurgical and Materials Transactions A, 2016, 47: 2773−2782.

[3] HE W L, MENG B, SONG B Y, WAN M. Grain size effect on cyclic deformation behavior and springback prediction of Ni-based superalloy foil [J]. Transactions of Nonferrous Metals Society of China, 2022, 32: 1188−1204.

[4] YANG W C, QU P F, LIU C, CAO K L, QIN J R, SU H J, ZHANG J, REN C D, LIU L. Temperature dependence of compressive behavior and deformation microstructure of a Ni-based single crystal superalloy with low stacking fault energy [J]. Transactions of Nonferrous Metals Society of China, 2023, 33: 157−167.

[5] GAO S, SONG Z F, HE B, ZHOU L Z, HOU J S. Effect of Ta addition on solidification microstructure and element segregation of IN617B nickel-base superalloy [J]. Transactions of Nonferrous Metals Society of China, 2022, 32: 559−568.

[6] WANG H P, LU P, CAI X, ZHAI B, ZHAO J F, WEI B. Rapid solidification kinetics and mechanical property characteristics of Ni−Zr eutectic alloys processed under electromagnetic levitation state [J]. Materials Science and Engineering: A, 2020, 772: 138660.

[7] ZHANG P C, WANG H P. Phase selection and characterization of Fe-based multi-component amorphous composite [J]. Materials Science and Engineering: A, 2022, 839: 142840.

[8] ZHANG K R, XIE F Q, HU R, WU X Q. Relationship between microstructure and mechanical properties of undercooled K4169 superalloy [J]. Transactions of Nonferrous Metals Society of China, 2016, 26: 1885−1891.

[9] LI S, LIU F, YANG W. Comparison of dendrite and dispersive structure in rapidly solidified Cu−Co immiscible alloy with different heat flow modes [J]. Transactions of Nonferrous Metals Society of China, 2017, 27: 227−233.

[10] LUO J, LUO H Y, ZHAO T S, WANG R Z. Effect of magnetic field on dislocation morphology and precipitation behavior in ultrafine grained 7075 aluminum alloy [J]. Journal of Materials Science and Technology, 2021, 93: 128−146.

[11] SHAO Q, WANG G, WANG H D, XING Z G, FANG C Y, CAO Q L. Improvement in uniformity of alloy steel by pulsed magnetic field treatment [J]. Materials Science and Engineering: A, 2021, 799: 140143.

[12] WANG F, QIAN D S, HUA L, MAO H J, XIE L C, SONG X D, DONG Z H. Effect of high magnetic field on the microstructure evolution and mechanical properties of M50 bearing steel during tempering [J]. Materials Science and Engineering: A, 2020, 771: 138623.

[13] LUO L, XIA H Y, LUO L S, SU Y Q, CAI C J, WANG L, GUO J J, FU H Z. Eliminating shrinkage defects and improving mechanical performance of large thin-walled ZL205A alloy castings by coupling travelling magnetic fields with sequential solidification [J]. Transactions of Nonferrous Metals Society of China, 2021, 31: 865−877.

[14] LUO T J, JI H M, CUI J, ZHAO F Z, FENG X H, LI Y J, YANG Y S. As-cast structure and tensile properties of AZ80 magnesium alloy DC cast with low-voltage pulsed magnetic field [J]. Transactions of Nonferrous Metals Society of China, 2015, 25: 2165−2171.

[15] ZUO X W, WANG E G, HAN H, ZHANG L, HE J C, Magnetic properties of Fe−49%Sn monotectic alloys solidified under a high magnetic field [J]. Journal of Alloys and Compounds, 2010, 492: 621−624.

[16] WANG J, HE Y X, LI J S, HU R, KOU H C, BEAUGNON E. Experimental platform for solidification and in-situ magnetization measurement of undercooled melt under strong magnetic field [J]. The Review of Scientific Instruments, 2015, 86: 025102.

[17] HE Y X, LIU X D, XING C X, BIAN Z C, ZHOU Q, WANG J, WANG H F, LI J S. Effect of long-term aging treatment on the tensile strength and ductility of GH605 superalloy [J]. Progress in Natural Science: Materials

International, 2022, 32: 375−384.

[18] NELL J M, GRANT N J. Multiphase strengthened nickel base superalloys containing refractory carbide dispersions [C]//Superalloys. Warrendale, PA: TMS, 1992: 113−121.

[19] WANG F, MA D, BÜHRIG-POLACZEK A. Micro-segregation behavior of alloying elements in single-crystal nickel-based superalloys with emphasis on dendritic structure [J]. Materials Characterization, 2017, 127: 311−316.

[20] JOHANNES R L, HAYDOCK R, HEINE V. Phase stability in transition-metal laves phases [J]. Physical Review Letters, 1976, 36: 372−376.

[21] WANG J, YUE S, FAUTRELLE Y, LEE P D, LI X, ZHONG Y B, REN Z M. Refinement and growth enhancement of Al_2Cu phase during magnetic field assisting directional solidification of hypereutectic Al−Cu alloy [J]. Scientific Reports, 2016, 6: 24585.

[22] LI L, LIANG W L, BAN C Y, SUO Y S, LV G C, LIU T, WANG X J, ZHANG H, CUI J Z. Effects of a high-voltage pulsed magnetic field on the solidification structures of biodegradable Zn−Ag alloys [J]. Materials Characterization, 2020, 163: 110274.

[23] LI L, XU B, TONG W P, HE L Z, BAN C Y, ZHANG H, ZUO Y B, ZHU Q F, CUI J Z. Directional growth behavior of α(Al) dendrites during concentration-gradient-controlled solidification process in static magnetic field [J]. Transactions of Nonferrous Metals Society of China, 2015, 25: 2438−2445.

[24] AN Y K, XU X L, ZHAO Y H, LU R P, DONG R F, ZHAO Z Y, HOU H. In situ observation of solidification velocity and refined structure transformation in nonequilibrium solidification of highly undercooled and single-phase alloys [J]. Journal of Materials Research and Technology, 2022, 16: 347−361.

[25] BU F, ZHANG Y Y, LIU H X, WANG J, BEAUGNON E, LI J S, HE Y X. Magnetic field intensity dependent micro-structure evolution and recrystallization behavior in a Co−B eutectic alloy [J]. Journal of Materials Science and Technology, 2023, 138: 93−107.

[26] PAN Y W, DONG A P, ZHOU Y, DU D F, WANG D H, ZHU G L, SUN B D. Enhanced strength-ductility synergy in a novel V-containing γ''-strengthened CoCrNi-based multi-component alloy [J]. Materials Science and Engineering: A, 2021, 816: 141289.

[27] AGNEW S R, HORTON J A, YOO M H. Transmission electron microscopy investigation of $\langle c+a \rangle$ dislocations in Mg and α-solid solution Mg−Li alloys [J]. Metallurgical and Materials Transactions A, 2002, 33: 851−858.

[28] GENÉE J, SIGNOR L, VILLECHAISE P. Slip transfer across grain/twin boundaries in polycrystalline Ni-based superalloys [J]. Materials Science and Engineering: A, 2017, 701: 24−33.

[29] MA Y, WANG Y X, CONG J Z, SUN Y. Magnetic-field tuning of hydrogen bond order-disorder transition in metal-organic frameworks [J]. Physical Review Letters, 2019, 122: 255701.

[30] QIU S, ZHANG X C, ZHOU J, CAO S, YU H, HU Q M, SUN Z M. Influence of lattice distortion on stacking fault energies of CoCrFeNi and Al−CoCrFeNi high entropy alloys [J]. Journal of Alloys and Compounds, 2020, 846: 156321.

[31] LU L, YOU Z S, LU K. Work hardening of polycrystalline Cu with nanoscale twins [J]. Scripta Materialia, 2012, 66: 837−842.

[32] SCHNEIDER M, LAPLANCHE G. Effects of temperature on mechanical properties and deformation mechanisms of the equiatomic CrFeNi medium-entropy alloy [J]. Acta Materialia, 2021, 204: 116470.

[33] ZHANG Z, JIANG Z H, XIE Y H, CHAN S L I, LIANG J M, WANG J. Multiple deformation mechanisms induced by pre-twinning in CoCrFeNi high entropy alloy [J]. Scripta Materialia, 2022, 207: 114266.

[34] YANG T, ZHAO Y L, TONG Y, JIAO Z B, WEI J, CAI J X, HAN X D, CHEN D, HU A, KAI J J, LU K, LIU Y, LIU C T. Multicomponent intermetallic nanoparticles and superb mechanical behaviors of complex alloys [J]. Science, 2018, 362: 933−937.

[35] WU X L, ZHU Y T, WEI Y G, WEI Q. Strong strain hardening in nanocrystalline nickel [J]. Physical Review Letters, 2009, 103: 205504.

[36] HE F, CHEN D, HAN B, WU Q F, WANG Z J, WEI S L, WEI D X, WANG J C, LIU C T, KAI J J. Design of $D0_{22}$ superlattice with superior strengthening effect in high entropy alloys [J]. Acta Materialia, 2019, 167: 275−286.

[37] ROEBUCK B, ALMOND E A, COTTENDEN A M. The influence of composition, phase transformation and varying the relative FCC and HCP phase contents on the properties of dilute Co−W−C alloys [J]. Materials Science and Engineering: A, 1984, 66: 179−194.

[38] ZHANG D D, ZHANG J Y, KUANG J, LIU G, SUN J. The $B2$ phase-driven microstructural heterogeneities and twinning enable ultrahigh cryogenic strength and large ductility in NiCoCr-based medium-entropy alloy [J]. Acta Materialia, 2022, 233: 117981.

[39] LIANG L, XU M F, CHEN Y H, ZHANG T M, TONG W, LIU H T, WANG H J, LI H X. Effect of welding thermal treatment on the microstructure and mechanical properties of nickel-based superalloy fabricated by selective laser melting [J]. Materials Science and Engineering: A, 2021, 819: 141507.

[40] PINEAU A, BENZERGA A A, PARDOEN T. Failure of metals I: Brittle and ductile fracture [J]. Acta Materialia, 2016, 107: 424−483.

利用磁场深过冷处理避免 GH605 合金强度−塑性的失衡

贺一轩[1,2,3,4]，卜 凡[1,2]，边张驰[1,2]，相明秀[1]，周蒙蒙[1]，刘栩东[1]，朱 雷[5]，王 军[1]，李金山[1]

1. 西北工业大学 凝固技术国家重点实验室，西安 710072；
2. 西北工业大学 先进密封材料与润滑研究中心，西安 710072；
3. 西北工业大学 上海创新协同中心，上海 201108；
4. 西北工业大学 超导材料与应用技术研究院，西安 710072；
5. 西安理工大学 陕西省电工材料与熔(浸)渗透技术重点实验室，西安 710048

摘 要：磁场下的过冷处理(UMF)是一类有效调控钴基合金微观结构和性能的方法。通过 UMF 处理同时提升 GH605 钴基高温合金的强度和塑性。结果表明，在 UMF 处理后，合金的晶粒显著细化，基体相固溶度增加，且合金的屈服强度提升。在原始锻态合金中，位错滑移为主要的变形机制；经过 UMF 处理后，多种变形机制如层错、孪生、位错滑移及其交互作用在压缩变形过程中被激活，导致合金的强度和塑性同时提高。此外，经 UMF 处理后，可获得沿晶界析出的硬质 Laves 相，该硬质相可有效阻碍压缩变形过程中裂纹的扩展。

关键词：过冷处理；磁场；GH605 合金；强化机制

(Edited by Xiang-qun LI)